

Three-year VLBI monitoring of PKS 0420–014

S. Britzen^{1,2}, A. Witzel¹, T.P. Krichbaum¹, R.M. Campbell³, S.J. Wagner⁴, and S.J. Qian^{1,5}

¹ Max-Planck-Institut für Radioastronomie, Auf dem Hügel 69, 53115 Bonn, Germany

² Present address: Netherlands Foundation for Research in Astronomy, Oude Hoogeveensedijk 4, 7991 PD Dwingeloo, The Netherlands

³ Joint Institute for VLBI in Europe, Oude Hoogeveensedijk 4, 7991 PD Dwingeloo, The Netherlands

⁴ Landessternwarte Königstuhl, 69117 Heidelberg, Germany

⁵ Beijing Astronomical Observatory, Chinese Academy of Sciences, Beijing 10080, P.R. China

Received 1 November 1999 / Accepted 15 May 2000

Abstract. We present nine 3.6-cm VLBI observations of the optically violent variable (OVV) flat-spectrum radio quasar PKS 0420–014 taken over a period of three years (1989.32–1992.48); we also show a VLBI map from observations at 43 GHz in 1992.4. We trace jet evolution and variability with individual components. We find superluminal motion with $\beta_{\text{app}} \sim 2\text{--}14c$ for five jet components. Components ejected more recently seem to separate faster from the core. All jet components follow one common curved path within the jet. In addition to presenting the results of the VLBI monitoring, we discuss a possible correlation between component ejection and outbursts seen in the radio/optical/gamma-ray regimes. The ejection of several jet components can be linked to flares in the cm-light curves; the most recently ejected component appeared shortly before a simultaneous radio/optical/gamma-ray flaring. Our results are in agreement with the predictions of the lighthouse model of Camenzind & Krockenberger (1992), which explains the observed optical flaring. We introduce an alternative model involving a precessing binary black hole.

Key words: techniques: interferometric – galaxies: quasars: individual: PKS 0420-014 – radio continuum: galaxies – gamma rays: theory

1. Introduction

VLBI monitoring of parsec-scale jets is a promising tool for studying the energy transport in AGN (active galactic nuclei) close to the central engine. The exact nature of this energy transport along the jets is still a question of debate. The jets of several AGN (3C 279, 3C 273, 3C 345, 1611+343, PKS 0528+134) have been studied extensively; such study has inspired a variety of scenarios involving jet-component motion. In addition to providing morphological information, VLBI monitoring, when compared to flux-density variability across the electromagnetic spectrum, can contribute towards understanding the physics of active nuclei. Dense sampling of the VLBI observations in time is important in order to match the temporal resolution of significant variability features as closely as possible. For instance, if a

source shows flaring with a characteristic timescale, we would ideally have several VLBI observations spanning this timescale to allow us to correlate meaningfully any light curve events with any derived structural evolution.

In order to study the kinematics of PKS 0420-014 in detail, we selected nine VLBI observations, spanning three years, from the geodetic data base. While the VLBI morphology of PKS 0420–014 is our principal interest, this source is also known for its pronounced flux-density variability in several regions of the electromagnetic spectrum, making it a likely candidate for the sort of analysis discussed above. In fact, PKS 0420–014 did undergo a simultaneous optical/gamma-ray flaring event at the time of a radio outburst, providing an opportunity to investigate the relation between the structural evolution and the flaring activity seen in the radio, optical, and gamma-ray regimes. In the following sections we give a brief overview of the flux-density variability recorded in the literature, report on previous VLBI observations of PKS 0420–014, present the VLBI monitoring results, and discuss relations between the radio morphology and the multi-wavelength flux-density variability. We also present two models, the lighthouse model and a binary black hole model (hereafter LH and BBH models, respectively), for PKS 0420–014. Wagner et al. (1995; hereafter W95) describe implications for emission processes and these rotating jet models for PKS 0420–014, making use of a subset of the VLBI observations presented here. We discuss the predictions of the LH model in the context of the full nine-epoch VLBI monitoring program. We also explain the VLBI results and the optical flaring behavior in the context of the BBH model. This is the second of three papers describing the astrophysical analysis of geodetic VLBI observations of three AGN (PKS 0528+134 (Britzen et al. 1999b), PKS 0420–014, and 1803+784 (Britzen et al. in prep.)).

2. Flux-density variability across the electromagnetic spectrum

2.1. Optical regime

Optical monitoring of PKS 0420–014 ($z = 0.915$, Kühr et al. 1981; $1 \text{ mas} \simeq 4.21h^{-1} \text{ pc}$, taking $H_0 = 100h \text{ km s}^{-1} \text{ Mpc}^{-1}$ and $q_0 = 0.5$ throughout) dates back to 1969. An optical light

curve presented by Webb et al. (1988) for the period December 1969–January 1986 shows the source to be active, with typical changes in brightness of 2–3 magnitudes on timescales of ~ 1 year. Strong variability (maximum $\Delta m \cong 2.8$ mag) is also seen in the 22-year light curve (1970–1992) reported by Clements et al. (1995). The strong optical variability is seen by Villata et al. (1997) and Raiteri et al. (1998) at later epochs. PKS 0420–014 had a historical maximum (14.15 mag in the R band) in its optical light curve on 15 September 1995 (Villata et al. 1997; Raiteri et al. 1998) and continued to show intense activity afterwards. Five years of optical monitoring within the Hamburg Quasar Monitoring Program and at the Landessternwarte in Heidelberg reveal two modes of variability at optical wavebands (W95): superimposed on an almost regular major flaring cycle having a timescale of ~ 13 months with each individual flare lasting about one month (peaks in early 1990, 1991 and 1992; see Fig. 10 and Table 6), are variations on shorter timescales.

2.2. Radio regime

PKS 0420–014 is variable from long-cm to short mm-wavelengths (Waltman et al. 1991; Tornikoski et al. 1993; Reich et al. 1993). It belongs to the group of variable extragalactic sources that has been monitored in total and polarized flux-density at radio frequencies (4.8–14.5 GHz) within the UMRAO programme (Aller et al. 1985). Fig. 8 shows the flux-density evolution between 1982 and 1994. In Table 6 we list the times when maxima are seen at different frequencies in the light curves. The observed flux density variations of about a factor of 2 on timescales of a few years are typical for highly polarized quasars (HPQs, Browne, 1989; W95). Reich et al. (1993) present observations between 2.695 GHz and 90 GHz using the Effelsberg 100-m and the IRAM 30-m telescopes. These observations were carried out shortly after (2–3 days) the Compton Gamma-Ray Observatory (CGRO, Fichtel et al. 1994) was observing this source. According to Fichtel et al., the source was “in a phase of decreasing radio emission but still at a quite high intensity at 90 GHz” during the period of CGRO detection. Observations by the Metsähovi Radio Research Station (Teräsanta et al. 1992) at 22 and 37 GHz reveal the flux-density of the source varying between 3 and 7 Jy on time scales of about 500 days. PKS 0420–014 has also been observed at 90, 142, and 230 GHz with the IRAM 30 m telescope (Reuter et al. 1997; Steppe et al. 1988, 1993). In Fig. 9 we show the mm-light curves for the time span 1985–1995.

2.3. Gamma-ray regime

Radecke et al. (1995) report the detection of gamma-ray emission in the energy range above 30 MeV from PKS 0420–014. EGRET detected gamma-radiation above 100 MeV during two observation periods in 1992: in viewing period 21 (two weeks, February 20 – March 5) and period 29 (three weeks, May 14 – June 4) (Hartman et al. 1992; 1999). An intensity decrease by a factor of at least 1.5 from a maximum of $5.0 \pm 1.4 \times 10^{-7}$ photons $\text{cm}^{-2}\text{s}^{-1}$ above 100 MeV was ob-

served during that time interval, indicating extreme variability (Radecke et al. 1995). Information about earlier pointings is given in Fichtel et al. (1994). PKS 0420–014 revealed its two highest gamma-ray fluxes ($5.02 \pm 1.04 \times 10^{-7}$ photons $\text{cm}^{-2}\text{s}^{-1}$ and $6.42 \pm 3.42 \times 10^{-7}$ photons $\text{cm}^{-2}\text{s}^{-1}$) in viewing period 21 and in viewing period 426 (August 8, 1995–August 22, 1995), respectively. In Fig. 11 we plot the gamma-ray observations from EGRET (Hartman et al. 1999) and show upper limits of the non-detections. W95 report on the simultaneity of the strong gamma-ray flaring in 1992 with a significant flaring in the optical regime, one of the first detections of such simultaneous events made in any source. The epoch of the viewing period 21 gamma-ray detection from PKS 0420–014 coincides with the strongest outburst of optical emission observed in 5 years of monitoring since 1989 (W95).

3. Previous radio interferometric observations

Antonucci & Ulvestad (1985) present VLA observations performed at 20 cm, in which PKS 0420–014 has an angular size of $42''$ (corresponding to a linear size of $177h^{-1}$ kpc) with a weak secondary component $\sim 20''$ to the northeast of the core and some extended emission to the south at separation $\sim 22''$. W95 present four epochs of geodetic VLBI observations performed at 8.4 GHz (a subset of the observations presented in this paper) that show superluminal motion ($\geq 3.9c$; ≥ 0.15 mas/yr) for at least one knot in the southern jet of PKS 0420–014 for the first time. The maps indicate motion along a curved, possibly helical trajectory. Model calculations incorporating the LH model (Camenzind & Krockenberger 1992) explain the optical flaring as being related to the ejection of new VLBI components. Shen et al. (1997) report results of a 5-GHz southern hemisphere VLBI survey using the SHEVE array plus the telescope at Shanghai from November 1992. The structure of PKS 0420–014 from these observations consists of a resolved core and a strong secondary component 0.96 mas south-west of the core at a position angle of -146° . Based on flux-density variability, they speculate about the ejection of a second component, which would have a putative proper motion of 0.15 mas yr^{-1} and thus would confirm the value in W95. VLBI observations of PKS 0420–014 at 2.32 and 8.55 GHz are presented by Fey et al. (1996), and at 5 GHz by Wehrle et al. (1992). Krichbaum et al. (1994) present the first ever 43-GHz map from observations at epoch 1992.40, revealing a core-jet structure oriented north-south and bending considerably (by more than 90°) near the core on mas to sub-mas scales (see Figs. 2, 3).

4. VLBI monitoring at 8.4 GHz (X-band)

We selected nine VLBI observations performed at $\lambda=3.6$ cm from the geodetic IRIS and IRIS-S database (International Radio Interferometric Surveying, S=South: Carter & Robertson 1984; Carter et al. 1988). The observations cover a period of more than three years and were chosen to be fairly evenly distributed through the whole time span. The last observation marks the time when the source was removed from the sample of

Table 1. Antenna abbreviations used in Table 2

Abbr.	Station	Country, (State)	Diameter [m]
H	Hartebeesthoek	South Africa	26
FD	Ft. Davis	USA, (TX)	25
M	Mojave	USA, (CA)	12
R	Richmond	USA, (FL)	18
S	Shanghai	China	25
WS	Westford	USA, (MA)	18
WT	Wetzell	Germany	20

Table 2. Details of the VLBI observations performed on PKS 0420–014

Exp.	Epoch	Antennas	Scans
IRIS540	1989.32	FD-R-WS-WT	104
IRIS-S26	1990.08	H-M-R-WS-WT	72
IRIS-S30	1990.38	H-M-R-WS-WT	112
IRIS-S40	1991.23	H-M-R-WS-WT	121
IRIS-S41	1991.31	H-M-R-WS-WT	108
IRIS-S47	1991.82	H-M-R-WS-WT	101
IRIS-S51	1992.15	H-M-R-WS-WT	110
IRIS-S54	1992.34	H-M-R-S-WS-WT	133
IRIS-S55	1992.48	H-M-R-WS-WT	48

geodetic VLBI sources. Details concerning the antennas participating in the observations and the abbreviations used for them are given in Table 2 and Table 1 respectively.

The observations were performed in the standard geodetic setup. A typical IRIS-S array comprises from 3 to 6 VLBI stations providing a resolution of ~ 0.5 mas and an almost circular beam. The data were recorded simultaneously at 2.3 and 8.4 GHz in the Mk III recording format. Details concerning the data export, calibration, and reduction are given in Britzen et al. (1999b). We performed the imaging with the standard procedures provided in the Caltech VLBI package. Starting from a point-source model, we mapped the source using the CLEAN algorithm. In order to quantify the source structure, we also fitted elliptical Gaussian components to the observed visibilities at each epoch. Depending on data quality and uv-coverage, we were able to fit models typically comprising from 5 to 8 Gaussian components within 3 mas from the core. We determined the errors of the individual parameters using formal error propagation in the least-square fits (program ERRFIT in the CalTech package). From previous experience with geodetic data analysis, i.e., by performing several model-fit calculations with different parameter sets and comparing the results, we realized that the errors calculated with ERRFIT may not be realistic for this kind of dataset. The following errors better reflect systematic effects in the elliptical Gaussian models: for the flux S , $\Delta S \sim 10\text{--}20\%$; for the distance r from the core, $\Delta r \sim 0.1$ mas; for the position angle Θ , $\Delta\Theta \sim 20\text{--}30^\circ$ for $r < 0.5$ mas, $\Delta\Theta \sim 5\text{--}10^\circ$ for $0.5 \text{ mas} < r < 2.5$ mas, and $\Delta\Theta \sim 10\text{--}20^\circ$ for $r > 2.5$ mas; and for the major axis $Ma.A.$, $\Delta Ma.A. \sim 0.1$ mas. Table 3 gives the results of the model-fitting procedure for all the components within 3 mas of core separation. The axial ratio is given by the

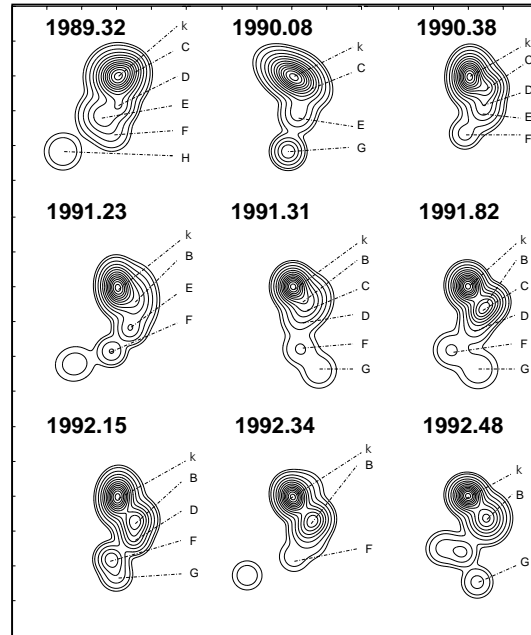


Fig. 1. Images based on gaussian model-fits obtained for nine epochs of VLBI observations of PKS 0420–014 at 8.4 GHz. Contour levels are 1, 2, 5, 10, 17, 25, 35, 45, 55, 65, 75, 85, and 95 percent of the peak brightness at each epoch. Tick marks are at 1 mas separation.

relation of the minor to major axis of the component, in most cases the components are circular (1.0).

Capital letters **A–H** denote individual elliptical Gaussian components from the model fits, labelled by increasing core separation (see Fig. 4). The core is labelled **k** (Table 3). The letter **x** (in Table 3) denotes jet features that only appear in one epoch and could not be reliably identified with a specific jet component; we disregard them in the following analysis.

5. Results

For the central 3-mas region, we show a composite picture of the model-fitting results for the nine selected epochs in Fig. 1. The overall source structure shows a jet comprising several components. The jet appears to bend twice, with the bending more pronounced nearer the core than farther away. This figure illustrates that the morphology of the jet changes from epoch to epoch due to the motion of jet components.

In Fig. 2 we show a hybrid map obtained at 43 GHz from global VLBI observations in May 1992 (Krichbaum et al. 1994). The source structure in this high resolution map confirms the structure seen in the 8.4-GHz observations. The map shows a curved jet which extends over ~ 10 mas towards the south. The resolution of these observations (beam: 0.99×0.17 mas; position angle: -6.93°) is significantly higher than that of the 8.4-GHz VLBI observations, and thus gives a detailed picture of the inner region of PKS 0420–014 not visible in the geodetic VLBI data. In Fig. 3 we redisplay the central region of the source, convolved with a circular beam of 0.3 mas to simplify the comparison with the other images. The bending continues even within

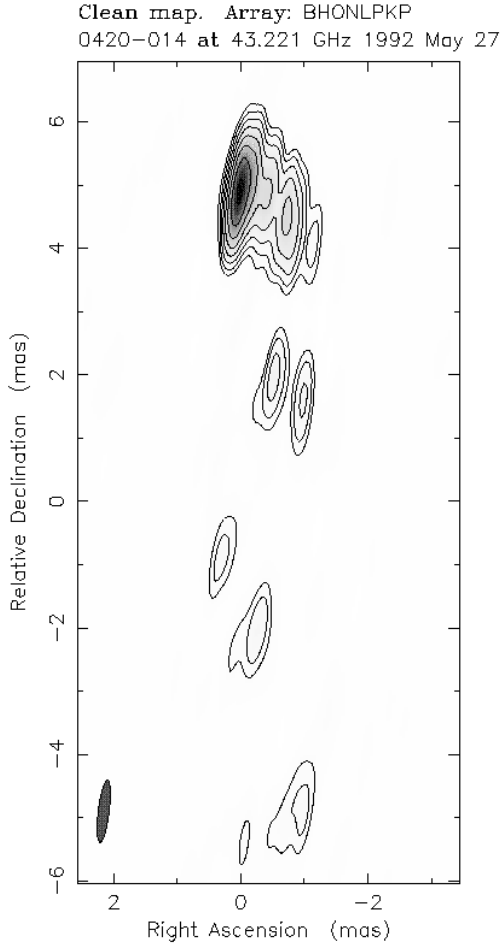


Fig. 2. Hybrid map of PKS 0420–014 at 43 GHz at epoch 1992.40. Contour levels are 0.7, 1.4, 2.8, 5.6, 11.2, 22.4, 44.8, and 89.6 percent of the peak flux density (2.39 Jy/beam). The beam is 0.99×0.17 mas at -6.93° .

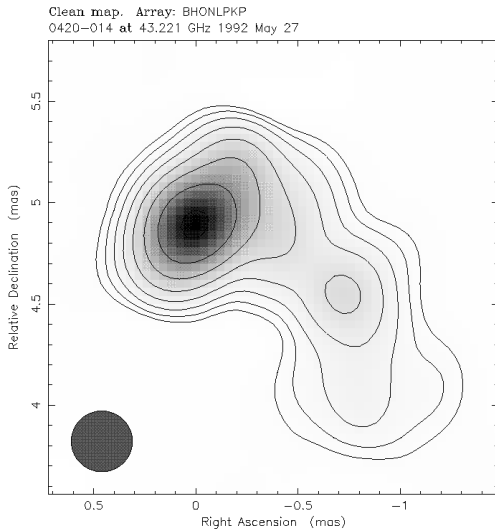


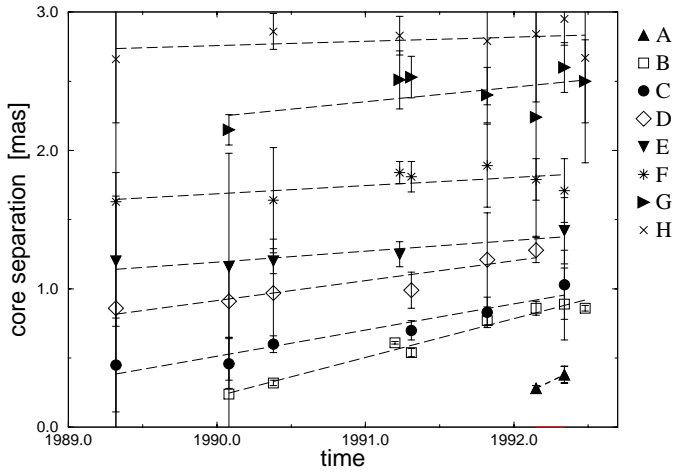
Fig. 3. Central region of the hybrid map shown in Fig. 2 convolved with a circular beam of 0.3 mas. Contours as in Fig. 2.

Table 3. Model-fit results for PKS 0420–014. We take as uncertainties $\Delta S \sim 10\text{--}20\%$, $\Delta r \sim 0.1$ mas, $\Delta\theta \sim 20\text{--}30^\circ$ for $r < 0.5$ mas, $\Delta\theta \sim 5\text{--}10^\circ$ for $0.5 \text{ mas} < r < 2.5$ mas, $\Delta\theta \sim 10\text{--}20^\circ$ for $r > 2.5$ mas, and $\Delta \text{Ma.A.} \sim 0.1$ mas. Components not shown or not labelled in Fig. 1 and their model-fit parameters are given in parentheses.

Epoch	Id.	S [Jy]	r [mas]	θ [$^\circ$]	Ma.A. [mas]	Axial ratio	
1989.32	k	2.3	0.00	0.00	0.6	1.0	
	C	0.2	0.45	303	0.1	1.0	
	D	0.2	0.86	187	0.2	1.0	
	E	0.5	1.20	159	0.5	1.0	
	F	0.1	1.63	175	0.4	1.0	
	H	0.1	2.66	144	0.5	1.0	
1990.08	k	2.0	0.00	0.00	0.9	0.4	
	(B)	0.1	0.24	300	0.4	(1.0)	
	C	0.1	0.46	254	0.3	0.9	
	(D)	0.1	0.91	192	0.3	(1.0)	
	E	0.1	1.16	187	0.3	1.0	
	G	0.2	2.15	177	0.1	0.8	
1990.38	k	2.0	0.00	0.00	0.5	0.4	
	(B)	0.1	0.32	304	0.4	(0.9)	
	C	0.6	0.60	239	0.2	0.9	
	D	0.4	0.97	206	0.3	1.0	
	E	0.1	1.20	193	0.4	1.0	
	F	0.1	1.64	176	0.2	0.9	
	(H)	0.1	2.86	174	0.4	(1.0)	
	(H)	0.1	2.83	168	0.4	(0.9)	
1991.23	k	1.8	0.00	0.00	0.5	0.4	
	B	0.8	0.61	237	0.8	0.5	
	E	0.2	1.25	196	0.1	0.8	
	F	0.1	1.84	175	0.1	0.8	
	(G)	0.1	2.51	151	0.7	(0.8)	
	(H)	0.1	2.83	168	0.4	(0.9)	
	1991.31	k	1.3	0.00	0.00	0.3	0.6
		B	0.5	0.54	234	0.5	1.0
C		0.3	0.70	211	0.4	1.0	
D		0.1	0.99	189	0.3	1.0	
F		0.1	1.81	187	0.4	1.0	
G		0.1	2.53	197	0.5	1.0	
1991.82		k	1.3	0.00	0.00	0.3	0.6
	B	0.5	0.77	232	0.2	0.8	
	C	0.5	0.83	205	0.1	0.9	
	D	0.1	1.21	189	0.3	1.0	
	F	0.1	1.89	165	0.4	1.0	
	G	0.1	2.40	187	0.6	1.0	
	(H)	0.1	2.79	172	0.3	(1.0)	
	(H)	0.1	2.79	172	0.3	(1.0)	
1992.15	k	1.7	0.00	0.00	0.5	0.3	
	(A)	0.1	0.28	300	0.4	(1.0)	
	B	0.9	0.86	217	0.4	0.8	
	D	0.3	1.28	201	0.1	0.9	
	F	0.3	1.79	174	0.1	0.9	
	G	0.1	2.24	179	0.2	0.9	
	(H)	0.1	2.84	174	0.4	(1.0)	
	(H)	0.1	2.84	174	0.4	(1.0)	

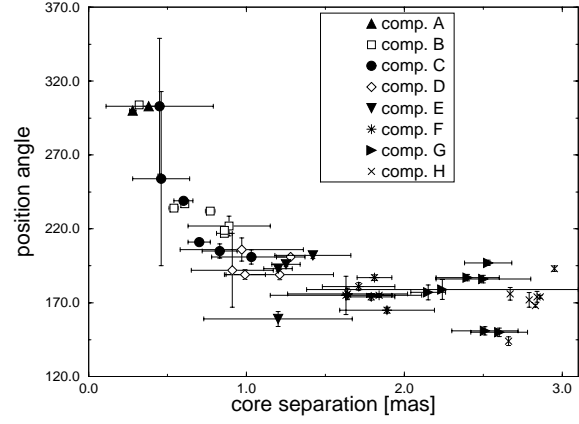
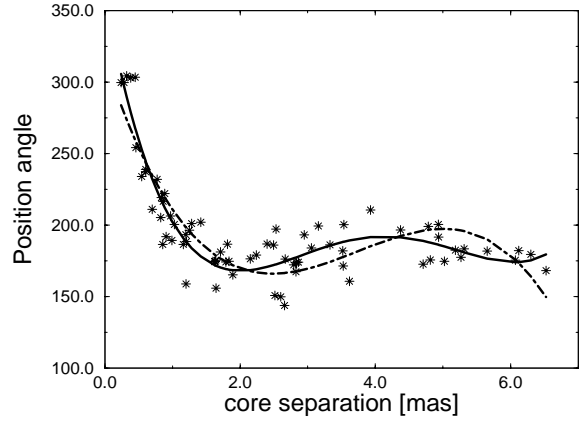
Table 3. (continued)

Epoch	Id.	S [Jy]	r [mas]	θ [$^\circ$]	Ma.A. [mas]	Axial ratio
1992.34	k	2.2	0.00	0.00	0.4	0.3
	(A)	0.2	0.38	303	0.5	0.9
	(B)	1.2	0.89	222	0.3	0.8
	(C)	0.3	1.03	201	0.2	0.9
	(E)	0.1	1.42	202	0.4	1.0
	(F)	0.1	1.71	181	0.4	0.9
	(G)	0.1	2.60	150	0.4	0.9
	(H)	0.1	2.95	193	0.4	0.9
1992.48	k	1.5	0.00	0.00	0.2	0.7
	B	1.1	0.86	219	0.5	0.8
	(x)	0.2	1.65	156	0.4	0.8
	(x)	0.2	1.63	175	0.1	0.8
	G	0.1	2.50	186	0.2	0.9
	(H)	0.1	2.67	176	0.5	0.8

**Fig. 4.** Jet component separation from the core versus time for individual components in PKS 0420–014. Symbols denote components as introduced in Table 3.

the innermost part, becoming even more pronounced with a $\sim 90^\circ$ turn at core separations < 0.5 mas.

Within the inner 3 mas from the core, we identified up to eight distinct jet components in the 8.4-GHz VLBI model fits. Assuming that the feature we identify as the core **k** in fact remains stationary, the individual components all move outwards and we can estimate meaningful separation velocities for each component as we follow them in time. Fig. 4 shows the separation of the components (**A–H**) from the core as a function of time. Nearly all of the outer components can be traced over the full three years, while the two innermost components **A** and **B** were ejected more recently. The positions of component **A** and **B** are consistent with the 43-GHz observations. Model fitting these data yields components at core separations of ~ 0.4 mas (component **A**) and ~ 0.8 mas (component **B**). Another jet component is seen at ~ 0.2 mas, but is beyond the resolution of the 8.4-GHz observations.

**Fig. 5.** Positions for individual jet components up to a core separation of ~ 3 mas, plotted as position angle versus separation from the core.**Fig. 6.** Positions for all jet components (including components at core separations > 3 mas) plotted as position angle versus core separation without error bars. Model-fit component paths are shown as solid line (fourth degree fit) and a dashed line (cubic fit).

We derived estimates for the separation speeds of the individual components by fitting straight lines to the model-fitted core separations as a function of time. These calculated separation speeds, as well as the parameters of the regression and the extrapolated time of ejection, are given in Table 4 for the components **A–G**. The uncertainty of the velocity for each component is taken to be the standard error of the slope. The velocity of component **A** had to be calculated on the basis of only two observations and is therefore subject to a correspondingly larger uncertainty. The uncertainty of the ejection time is taken to be the corresponding uncertainty in the time-axis intercept due to the velocity uncertainty. Due to resolution effects, the uncertainties of the radial distances for the components beyond component **F** are smaller than the uncertainties of the position angles (see Figs. 5, 6). We do not include these components in the discussion of the separation velocities. For the rest, we find that the more recently ejected components have faster separation speeds.

We show the position angle Θ of the component relative to the core versus the core separation for components **A–H** in Fig. 5. Despite some larger error bars, the general trend is that

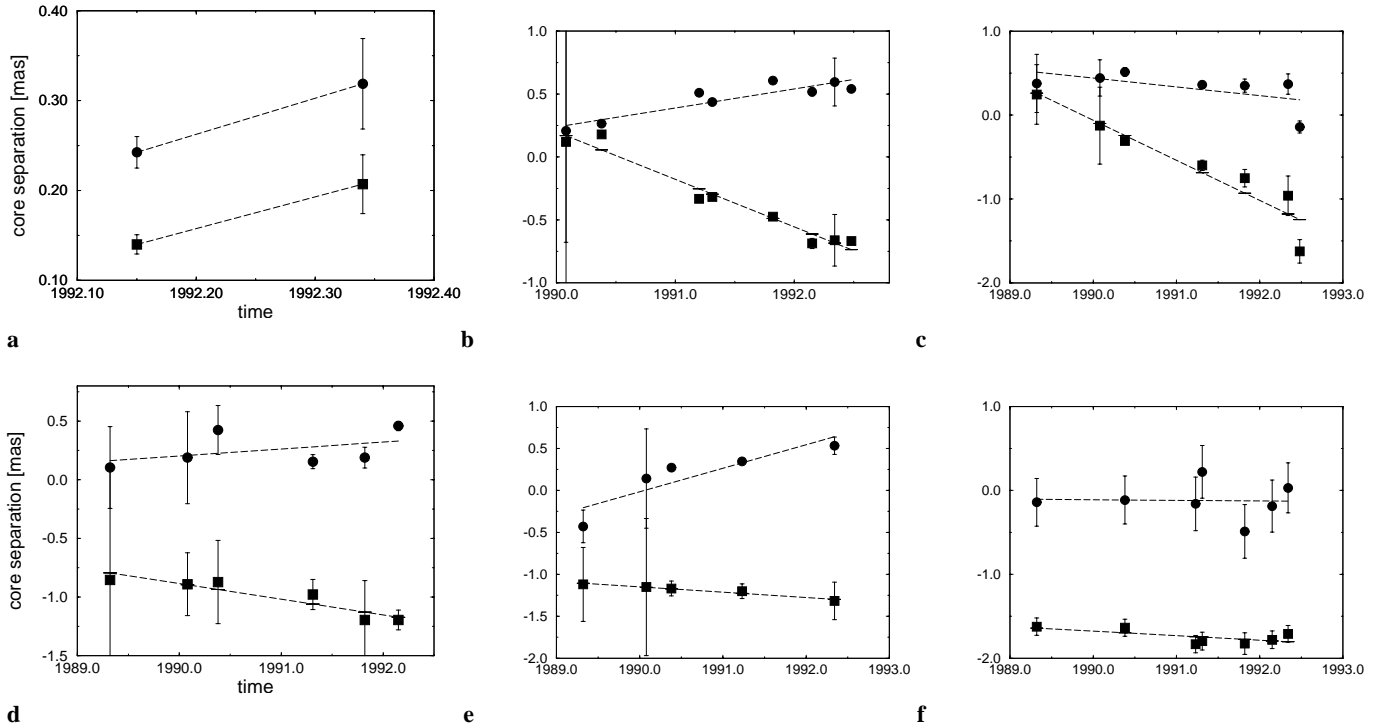


Fig. 7a–f. The figures **a–f** show the core separations for components **A–F**, plotted in rectangular coordinates ($X(t) = \cos\delta\Delta\alpha(t)$, filled circles; $Y(t) = \Delta\delta(t)$, filled squares) as a function of time. In addition, we show a linear regression fit (dashed line) to the motion in each coordinate. The parameters of the regression are given in Table 5.

Table 4. β_{app} , polynomial coefficients (A_0 , A_1) derived from linear regression, and inferred ejection times from the core. We used the following cosmological parameters for our calculations: $H_0 = 100 \text{ km s}^{-1} \text{ Mpc}^{-1}$, $q_0 = 0.5$.

Comp.	$\beta_{\text{app}}[c]$	A_1 [mas/year]	A_0 [mas]	time of ejection ($-A_0/A_1$)
A	13.8 ± 8.7	0.5263158	-1048.22	1991.6 ± 0.3
B	7.4 ± 0.5	0.2802028	-557.3793	1989.2 ± 0.6
C	5.0 ± 0.7	0.1893678	-376.3292	1987.3 ± 1.0
D	3.8 ± 0.7	0.1437679	-285.1828	1983.6 ± 1.5
E	2.1 ± 0.6	0.0782125	-154.4493	1974.7 ± 2.0
F	1.6 ± 0.9	0.05923992	-116.2012	1961.5 ± 4.0
G	2.8 ± 2.0	0.1061696	-209.032	1968.8 ± 5.0

all the components seem to follow one common path. If we include the information from the 43-GHz hybrid map, the path starts at a position angle of $\sim 340^\circ$ and bends towards a position angle of $\sim 300^\circ$ at a core separation < 0.5 mas (Bend 1), then bends towards a position angle of $\sim 180^\circ$ at a core separation of ~ 1.5 – 2 mas (Bend 2). Fig. 6 illustrates the complete jet ridge line, incorporating all jet features we detected. This figure and Fig. 6 suggest that the jet bends again at core separations of 4–5 mas (Bend 3). To guide the eye, we plot third- and fourth-degree regression polynomials.

We present the motion parametrized in rectangular coordinates $X(t)$ and $Y(t)$ in Fig. 7 and give the parameters of this linear fit in Table 5, where we have also calculated the resulting

separation speeds. These speeds seem to disagree with those listed in Table 4 for components **B** and **C**, and seem to agree quite well for components **A** and **D**. The most obvious reason for the difference is the curvature which is taken into account in the calculations in Table 5. The curvature is largest for components **B** and **C** and is less for component **D**. The velocity of component **A**, based on only two data points, does not yet have any sensitivity to curvature of the jet.

In Fig. 8 we show the flux-density evolution at cm-wavelengths (2.1, 3.6, and 6 cm). The flux-density data were kindly provided by the UMRAO programme. The radio flux-density evolution is characterized by significant outbursts spaced at roughly one to three year intervals. Outbursts occur at all three frequencies. Typically an outburst is seen to start earlier at higher frequencies (see Aller et al. 1985). Fig. 9 shows the flux-density evolution in PKS 0420–014 at mm-wavelengths (Steppe et al. 1993; Reuter et al. 1997). We show observations in the frequency range 87.70–90.13 GHz (called 3 mm in Table 6), 142.30–150.99 GHz (called 2 mm in Table 6), and 221.4–233.7 GHz (called 1.3 mm in Table 6). Fig. 10 shows the optical light curve published in W95. In Fig. 11 we plot the gamma-ray observations and upper limits of the non-detections from EGRET (Hartman et al. 1999). In Fig. 12 we show the core separation versus time for the two most recently ejected components **A** and **B** (a detail from Fig. 4).

In Table 6 we summarize times associated with flares visible in the light curves at different wavelengths (tabulated as year – 1900 with the uncertainty below, both in bold face). In addition,

Table 5. Coefficients of the linear regression fits to the parametrized $X(t)$ and $Y(t)$ component paths shown in Fig. 7 ($X(t)=V_x \cdot t + x_0$; $Y(t)=V_y \cdot t + y_0$; and $V_{\text{tot}} = \sqrt{V_x^2 + V_y^2}$).

Ident.	V_x [mas/year]	V_y [mas/year]	x_0 [mas]	y_0 [mas]	V_{tot} [mas/year]	β_{app} [c]
A	0.401053	0.352632	-0.0868832	-0.03527015	0.53	13.94
B	0.1510572	-0.3771428	-300.3656	750.7134	0.41	10.78
C	-0.1045611	-0.4773003	208.5167	949.7648	0.49	12.89
D	0.05927368	-0.1336172	-117.7509	265.0136	0.15	3.95
E	0.2799963	-0.06361887	-557.2086	125.4524	0.29	7.63
F	-0.007144846	-0.05422974	14.10657	106.2399	0.05	1.31

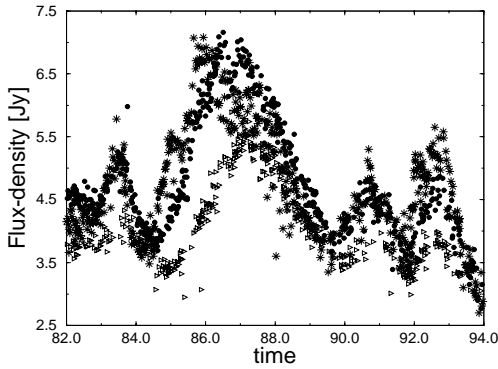


Fig. 8. Flux-density evolution between 1982 and 1994 at 14.5 GHz (stars), 8 GHz (filled circles), and 4.8 GHz (open triangles) (UMRAO programme).

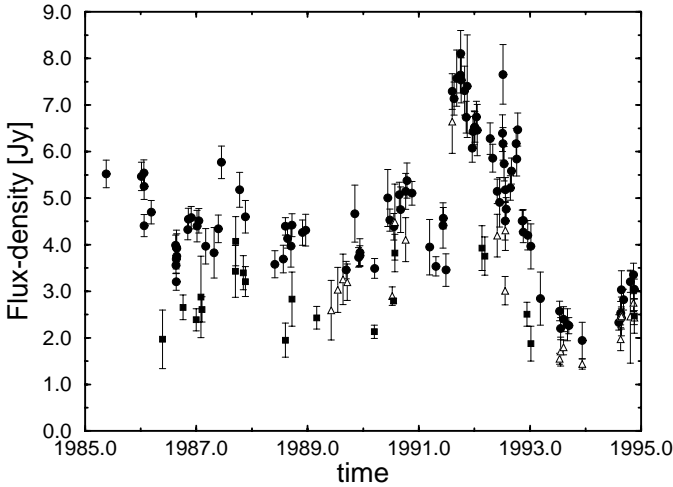


Fig. 9. Flux-density observations obtained with the 30m MRT at Pico Veleta at three different wavelength ranges (see text): 3 mm (filled circles), 2 mm (open triangles), and 1.3 mm (filled squares) (Steppe et al. 1993; Reuter et al. 1997).

we give the starting times (below the peak times) for the flares in the cm light curves. Events whose identification as flares is less certain are given in brackets. For our analysis we concentrate on the following monitoring periods: 1982–1993 for 4.8–14.5 GHz, 1986–1993 for 1.3–3 mm, 1990–1993 for optical, and 1991–1993 for gamma rays. The flaring behaviour is complex, with several events occurring during the monitoring periods. In

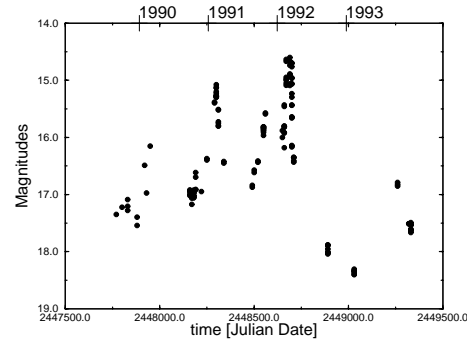


Fig. 10. Light curve of PKS 0420–014 at 650 nm (errors are smaller than symbols) (W95).

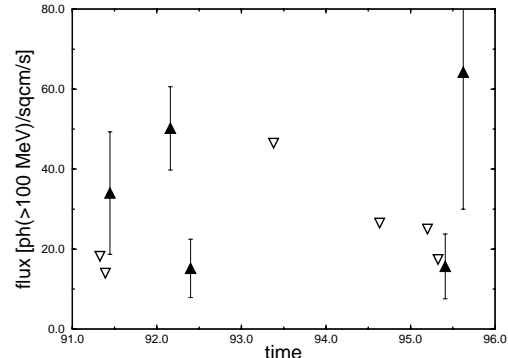


Fig. 11. Light curve of PKS 0420–014 in the range 100 MeV – 5 GeV (Hartman et al. 1999). Upper limits are displayed as empty triangles. The plotted time of observation is the center of the viewing period.

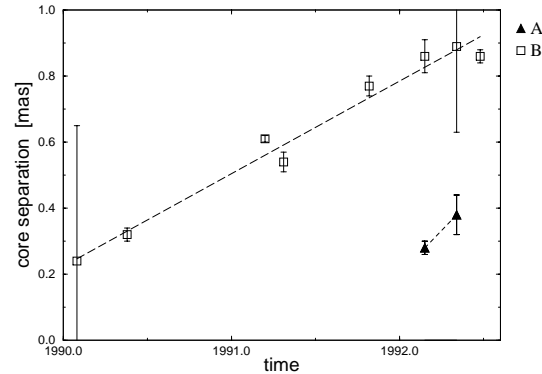


Fig. 12. Core separation versus time for component **A** and **B** and dashed lines indicating the linear regression.

Table 6. A summary of the times of outbursts observed at different frequencies in the respective monitoring periods (see text). The dates were determined from the light curves shown in Fig. 8–11.

λ	1983	1984	1985	1986	1987	1988	1989	1990	1991	1992
4.8 GHz	83.6				87.1			90.9		92.5
	± 0.2				± 0.3			± 0.2		± 0.2
start of flare					84.8			89.9		91.8
					± 0.2			± 0.2		± 0.1
8 GHz	83.6			86.5	87.0			90.8		92.7
	± 0.2			± 0.3	± 0.1			± 0.2		± 0.2
start of flare	82.8			84.5				89.8		91.9
	± 0.3			± 0.2				± 0.2		± 0.1
14.5 GHz	83.4	84.9	85.8		[87.4]			90.5		92.5
	± 0.2	± 0.1	± 0.2		± 0.2			± 0.2		± 0.3
start of flare	82.7	84.2						89.4		91.8
	± 0.3	± 0.2						± 0.3		± 0.2
3 mm					[87.5]	[88.8]	[89.9]	90.8	91.8	[92.5]
					+0.3, -0.1	± 0.1	+0.1, -0.2	± 0.1	± 0.1	± 0.1
2 mm							[89.6]	[90.6]	91.6	[92.6]
							± 0.1	+0.2, -0.1	± 0.8	+0.9, -0.1
1.3 mm					[87.7]	[88.7]				
					+0.2, -0.1	+0.5, -0.1				
650 nm								90.16	91.12, [91.82]	92.18
								+0.58, -0.05	± 0.01 ; +0.26, -0.01	+0.01, -0.06
> 100MeV										92.16
										+0.24, -0.71

addition, a given event may have peaked at different times at different wavelengths (see also Stevens et al. 1994, 1995). As an example, at cm-wavelengths we see a major flare starting in ~ 1984 and peaking first at 14.5 GHz (1985.8), then at 8 GHz (1986.5), and finally at 4.8 GHz (1987.1). In 1990/91 another (small) flare at cm-wavelengths is observable; this was probably the same flare occurring at mm-wavelengths in 1990. Similarly, at mm-wavelengths a large event peaked in late 1991; this flare is seen at cm-wavelengths at a time around 1992.5. The decline of this mm-flare was interrupted by another event visible in the 3 mm and 2 mm data that peaked in late 1992 and subsequently decayed through 1993 (see Stevens et al. 1995 for discussion of the second flare at high frequencies). The rise of the 1992 cm-radio outburst seems to be accompanied by a gamma-ray flare that might have peaked earlier than the cm-radio flare. The maximum in the gamma-ray light curve in 1992.16 was followed by a much smaller flux-density value. The highest gamma-ray flux density coincided with the highest flux-density value of the optical flaring (W95).

6. Discussion

In the previous sections we presented ten VLBI observations, including the 43-GHz observations, of PKS 0420–014 spanning three years. In the present section, we will discuss the correlation between epochs of component ejections and multi-frequency flux-density flares, as well as the kinematics of the jet components and jet morphology. We will further discuss theoretical models that can explain observed morphological features as well as some of the observed flux-density flaring events seen in some bands.

6.1. Correlations between component ejections and broad-band-flaring

In the following, we discuss the ejection times for jet components in PKS 0420–014 with respect to the flaring events observed in several wavelength bands. In Table 4 we list putative ejection times for individual jet components. In Table 6 we summarize the times associated with flares observed at different frequencies. Because of the uncertainties in the computed jet component ejection times, the undersampling of the light curves, and the rapid variability of PKS 0420–014 in the mm, optical and gamma-ray regimes, it is not possible to correlate component ejection times with flux density variability at those wavelengths reliably. The much better sampling at cm radio wavelengths makes it possible to relate component ejection times to events in the cm radio light curves. However, these correlations are somewhat limited by any unmodelled accelerations in the jet.

- component **D** was ejected at a time (1983.6 ± 1.5) that correlates quite well with the 1983 flare in the cm-wavelength curves (see Fig. 8). The error associated with the ejection time prevents us from saying whether the component was ejected before, during, or after the observed flaring.
- component **C** was ejected at a time (1987.3 ± 1.0) that might correlate with the time of the major flare at cm wavelengths (see Fig. 8).
- component **B** was ejected at a time (1989.2 ± 0.6) that correlates well with the minimum in the cm-wavelength curves (see Fig. 8) preceding the 1990-flare at cm wavelengths.
- component **A** was ejected at a time (1991.6 ± 0.3) that correlates well with the minimum in the cm-wavelength curves (see Fig. 8) preceding the large 1992 flare at cm wavelengths.

Our data yield evidence for different sorts of correlation between the instances of component ejection and flux-density variability. Component ejection can be simultaneous to maxima in the cm-light curve (ejection of component **C** and possibly **D**). For component **A** and **B** the time of ejection coincides with a minimum before occurrences of enhanced flux-density activity in the cm-radio bands. Though specific correlations with mm, optical, and gamma-ray events could not be reliably made due to insufficiencies in the data for PKS 0420–014, inspection of the light curves for those regimes reveals flares near the computed ejection times that might be related to the ejection in a way that is consistent with those reported for some other sources: e.g., NRAO 530 (Bower et al. 1997), 1611+343 (Piner & Kingham 1997), 3C 273 (Krichbaum et al. 1998), and PKS 0528+134 (Krichbaum et al. 1995, Britzen et al. 1999b). These references report a sequence of ejection of VLBI components from the core following a high-energy outburst, which in turn could be traced through to lower energy bands. In the superluminal quasar 3C 279 there are ejections of VLBI components nearly coincident with gamma-ray flaring (Wehrle et al. 1994). The gamma-ray emission detected in a large number of blazars (von Montigny et al. 1995) is most likely produced by inverse-Compton scattering from relativistic jet electrons and is Doppler boosted via beaming toward us, although the details of this process are not yet clear. One of several alternative explanations is that the gamma-ray bursts might be related to precessing relativistic e^\pm beams (Roland et al. 1994).

W95 speculate that the three bumps seen in the 37-GHz data separated by about 13 months (Stevens et al. 1994) might correspond to the three optical peaks, if a delay of 9 months is assumed. Radio-optical connections have been claimed for some well-monitored individual events in PKS 0420–014 (Dent et al. 1979). It is not clear to us whether there is a correlation between the optical flaring and the radio outbursts for PKS 0420–014 in general. It is possible that the simultaneous optical/gamma event correlates with the radio outburst in 1992, but we have no evidence for any further correlation between the radio and the optical. Although PKS 0420–014 has been monitored in the optical and radio regimes for about 20 years, the spacing of observations in both regimes limits the correlation studies between the radio and the optical light curves for the whole period (Clements et al. (1995), Tornikoski et al. 1994).

6.2. Kinematics

Our data yield evidence for up to eight distinct components in the jet of PKS 0420–014. Five jet components can be traced over the whole time range of our observations, components **B** and **G** can be seen in all but the first epoch, and the most recently ejected component (**A**) is seen only in two epochs. The components separate from the core with superluminal velocities between $7.4\text{--}1.6c$ for components **B–F** and $\sim 14c$ for component **A**. The speeds of component **B–F** fall in a range typical for individual components in superluminal sources (e.g., Vermeulen & Cohen 1994; Britzen et al. 1999a). Our observations indicate that the younger (more recently ejected) components tend to move faster than do the older components (see Fig. 4 and Table 4).

Our VLBI observations begin to detect jet components at position angles of roughly 300° relative to the core in the region within 0.5 mas from the core (see Fig. 5, 6). As the jet components separate from the core, they move along a curved trajectory towards a position angle of $\sim 180^\circ$ (by ~ 2 mas core separation). From here the position angle of the jet increases again and the jet bends towards a position angle of $\sim 200^\circ$ at a core separation of $\sim 4\text{--}5$ mas. All the different components follow identical paths along the twice-bent jet (see Fig. 5, 6). The path is curved by at least 120° within the inner 2 mas at an observing frequency of 8.4 GHz. The 43-GHz VLBI image detects jet components closer to the core. A first jet component (not visible in the 8.4 GHz images) appears at a core separation of ~ 0.2 mas and position angle of $\sim 340^\circ$. This indicates, as already shown in Krichbaum et al. (1994) that at higher frequencies the jet bending in PKS 0420–014 is even more pronounced than seen in the 8.4-GHz observations. At 43 GHz, the components seem to move on a similar path. This leads to the assumption that the total bending within the inner 2 mas must be at least $\sim 160^\circ$. Taking curvature into account when calculating velocities along the jet leads to higher velocity values, as can be seen by comparing Table 4 and 5 for the case of components **B** and **C**, which are the most affected by the jet curvature.

Rarely are the reported motions in AGN along straight trajectories: kinks and bends are frequently seen in the cm regime as well as in the mm regime (Krichbaum et al. 1994 for PKS 0528+134, PKS 0420-014, 1803+784; Krichbaum et al. 1995 for 3C 454.3). In a small number of cases, complicated curved trajectories have been determined (Zensus 1997 and references therein). In contrast to our results for PKS 0420–014, Zensus (1997) has measured different apparent trajectories for the superluminal features in 3C 345 within 1 mas of the stationary core. In this and other sources (e.g., PKS 0528+134, Britzen et al. 1999b), the curvature appears most pronounced near the core, similar to PKS 0420–014.

Our results presented above confirm predictions of the LH model for PKS 0420-014 (W95). Magnetic fields are a necessary element for jet formation; dynamo action in the inner accretion disk creates a rotating magnetosphere that is filled with disk plasma (Camenzind & Krockenberger 1992). The superposition of the outflow and the rotational motion of the jet plasma results in a helical trajectory. Thus, motion on helical trajec-

ries is expected in sources with highly relativistic, magnetized jets. The velocity vector of the knot sweeps around the jet axis, producing a time-dependent Doppler boosting for an observer along a fixed line-of-sight. The interplay between the helical trajectory and variable Doppler boosting leads to a “lighthouse-effect”. The LH model of relativistic magnetized jets is able to explain qualitatively the symmetry and similarity of subsequent optical outbursts in 1990–1992 (see Fig. 10). Components moving with apparent superluminal velocities on a curved trajectory seen in our VLBI observations support the model. The model predicts that the repeated optical flares were caused by a knot ejected in 1991, which our VLBI observations can identify as component **A**. Our result that several jet components move with superluminal speeds on the same path is also in agreement with the LH model.

A number of other geometrical models based on helical motion have been proposed to explain the curved quasiperiodic trajectories seen in 3C 345, 1803+784, 4C39.25, and similar sources (Steffen et al. 1995; Qian et al. 1991, 1996). Models incorporating magnetic fields have been introduced by Camenzind (1986) and Königl & Choudhuri (1985). Helical motion can also be readily explained from three-dimensional Kelvin-Helmholtz jet simulations (Hardee 1987; Hardee et al. 1995). A precession in the region of the nucleus (Blandford 1987), for example caused by gravitational interaction between galaxies, binary black holes, or black-hole/disk systems, can explain the apparent bending of jets and jet components moving on different trajectories, as well as components moving on the same curved trajectory (see Abraham & Carrara 1998 for the precessing jet in 3C 279). Binary black holes have been postulated to be responsible for jet wiggling on pc-scales (see Roos et al. 1993 for 1928+738) and for observed periodic optical flaring (Valtonen et al. 1999 for OJ287). A model by Britzen et al. (in prep.) postulates a binary black hole in the center of PKS 0420–014. They propose that the gravitational influence of a binary system causes the precession of an accretion disk as well as the motion of the black hole ejecting the plasma. A perturbation of the magnetic field lines due to the precessing accretion disk in turn perturbs the relativistic e^\pm beam that is assumed to move along them. Britzen et al. (in prep.) show that the results of the VLBI monitoring presented in this paper — the paths and motions of the jet components — can be explained within the framework of a binary black hole system. In addition, they show that the outburst in the optical light curve associated with the ejection of a new VLBI component can be explained by the motion of the black hole that is responsible for the jet and jet components. In this scenario, the amplitude of the optical peaks is very sensitive to the ratio of the masses in the binary system.

7. Conclusions

We have presented nine VLBI observations of the OVV quasar PKS 0420–014 performed at $\lambda=3.6$ cm between 1989.32 and 1992.48. The jet can be well described by up to eight distinct jet components. We have detected apparent superluminal motion between $\sim 2\text{--}14c$ for five jet components. The components

seem to separate faster in the vicinity of the core; the “older” jet components in PKS 0420–014 move more slowly. All components move on the same path along a twice-bent, strongly curved jet. Global VLBI observations performed at 43 GHz presented in this paper indicate a similar path for the jet components. The bending continues towards the innermost part, becomes even more pronounced with a $\sim 90^\circ$ turn at core separations < 0.5 mas. Therefore, the total bending within the inner 2 mas must be at least $\sim 160^\circ$. We extrapolated each component’s trajectory back to the time of its ejection. We have discussed the correlation between epochs of component ejection and multi-wavelength flux-density activity. We found that times of ejection agree well with times preceding enhanced flux-density activity in the cm regime for two components **A** and **B**. Though less frequent sampling prevent reliable correlation analysis, inspection of the light curve suggests these ejection times may also occur during times of maxima in the mm regime for the three components **A**, **B**, and **C**. Component **B** seems to have been ejected during the minimum before the 1991 radio-flare, and component **A** before the simultaneous optical/gamma-ray flaring in 1992, which appeared during an outburst in the radio regime. Our observations are consistent with predictions of the LH model for the VLBI jet morphology and kinematics, originally made to explain the quasi-periodic optical flaring. A paper describing an alternative model assuming a BBH system in the center of PKS 0420–014 is in preparation (Britzen et al. in prep.).

Acknowledgements. Special thanks are due to an anonymous referee whose meticulous reading of the manuscript helped to improve the paper substantially. This research has made use of data from the University of Michigan Radio Astronomy Observatory which is supported by the National Science Foundation and by funds from the University of Michigan. We thank M. and H. Aller for communicating data prior to publication. We thank R. Hartman, H. Ungerechts and U. Lisenfeld for supplying in part unpublished data. We are thankful to A. Lobanov and A.-M. Gontier for useful discussions, A. Müskens for help with the data export, and G. Hampson for significantly improving the layout of this work. Part of this work was supported by the European Commission, TMR Programme, Research Network Contract ERBFMRXCT97-0034 CERES.

References

- Abraham Z., Carrara E.A., 1998, *ApJ* 496, 172
 Aller H.D., Aller M.F., Latimer G.E., Hodge P.E., 1985, *ApJS* 59, 513
 Antonucci R.R.J., Ulvestad J.S., 1985, *ApJ* 294, 158
 Bower G.C., Backer D.C., Wright M., et al., 1997, *ApJ* 484, 118
 Blandford R.D., 1987, In: Zensus J.A., Pearson T.J. (eds.) *Superluminal Radio Sources*. Cambridge Univ. Press, Cambridge, p. 310
 Britzen S., Vermeulen R.C., Taylor G.B., et al., 1999a, In: Takalo L.O., Sillanpää A. (eds.) *BL Lac Phenomenon*. PASP Conference Series 159, p. 431
 Britzen S., Witzel A., Krichbaum T.P., et al., 1999b, *A&A* 341, 418
 Browne I.W.A., 1989, In: Maraschi L., Maccacaro T., Ulrich M.-H. (eds.) *BL Lac Objects*. Springer-Verlag, Berlin, New York, NY, p. 401
 Camenzind M., 1986, *A&A* 156, 137
 Camenzind M., Krockenberger M., 1992, *A&A* 255, 59
 Carter W.E., Robertson D.S., 1984, In: *International Symposium on Space Techniques for Geodynamics*. Sopron, Hungary, Magyar Tudományos Akademia Geodeziai es Geofizikai Kutato Intezet, Volume 1 (A86-29426 12-46), p. 214
 Carter W.E., Robertson D.S., Nothnagel A., et al., 1988, *JGR* 93, 14947C
 Clements S.D., Smith A.G., Aller H.D., Aller M.F., 1995, *AJ* 110, 529
 Dent W.A., Balonek T.J., Smith A.G., Leacock R.J., 1979, *ApJ* 227, L9
 Fey A.L., Clegg A.W., Fomalont E.B., 1996, *ApJS* 105, 299
 Fichtel C.E., Bertsch D.L., Chiang J., et al., 1994, *ApJS* 94, 551
 Hardee P.E., 1987, *ApJ* 318, 78
 Hardee P.E., Clarke D.A., Howell D.A., 1995, *ApJ* 441, 644
 Hartman R.C., Bertsch D.L., Fichtel C.E., 1992, *IAU Circ.* 5519, 1
 Hartman R.C., Bertsch D.L., Bloom S.D., et al., 1999, *ApJS* 123, 79
 König A., Choudhuri A.R., 1985, *ApJ* 289, 173
 Krichbaum T.P., Standke K.J., Witzel A., et al., 1994, In: Kus A.J., Schilizzi R.T., Borkowski K.M., Gurvits L.I. (eds.) *Proceedings of the 2nd EVN/JIVE Symposium*. Torun, Torun Radio Astronomy Observatory, p. 47
 Krichbaum T.P., Britzen S., Standke K.J., et al., 1995, *Proc. Natl. Acad. Sci. USA* 92, 11377
 Krichbaum T.P., Kraus A., Otterbein K., et al., 1998, In: Zensus J.A., Taylor G.B., Wrobel J.M. (eds.) *Proc. IAU Colloquium 164, Radio Emission from Galactic and Extragalactic Compact Sources*. PASP Conference Series 144, p. 37
 Kühr H., Witzel A., Pauliny-Toth I.I.K., Nauber U., 1981, *A&AS* 45, 367
 Piner B.G., Kingham K.A., 1997, *ApJ* 479, 684
 Qian S.J., Krichbaum T.P., Witzel A., et al., 1991, *Acta Astro. Sin.* 32(4), 369; *Transl. Chin. Astron. Astrophys.* 16, 137
 Qian S.J., Krichbaum T.P., Zensus J.A., et al., 1996, *A&A* 308, 395
 Radecke H.-D., Bertsch D.L., Dingus B.L., et al., 1995, *ApJ* 438, 659
 Raiteri C.M., Ghisellini G., Villata M., et al., 1998, *A&AS* 127, 445
 Reich W., Steppe H., Schlickeiser R., et al., 1993, *A&A* 273, 65
 Reuter H.-P., Kramer C., Sievers A., et al., 1997, *A&AS* 122, 271
 Roland J., Teyssier R., Roos N., 1994, *A&A* 290, 357
 Roos N., Kaastra J.S., Hummel C.A., 1993, *ApJ* 409, 130
 Shen Z.-Q., Wan T.-S., Moran J.M., et al., 1997, *AJ* 114, 1999
 Steffen W., Zensus J.A., Krichbaum T.P., et al., 1995, *A&A* 302, 335
 Steppe H., Salter C.J., Chini R., et al., 1988, *A&AS* 75, 317
 Steppe H., Paubert G., Sievers A., et al., 1993, *A&AS* 102, 611
 Stevens J.A., Litchfield S.J., Robson E.I., et al., 1994, *ApJ* 437, 91
 Stevens J.A., Litchfield S.J., Robson E.I., et al., 1995, *MNRAS* 275, 1146
 Teräsranta H., Tornikoski M., Valtaoja E., et al., 1992, *A&AS* 94, 121
 Tornikoski M., Valtaoja E., Teräsranta H., et al., 1993, *AJ* 105, 1680
 Tornikoski M., Valtaoja E., Teräsranta H., et al., 1994, *A&A* 289, 673
 Valtonen M.J., Lehto H.J., Pietilä H., 1999, *A&A* 342, L29
 Vermeulen R.C., Cohen M.H., 1994, *ApJ* 430, 467
 Villata M., Raiteri C.M., Ghisellini G., et al., 1997, *A&AS* 121, 119
 von Montigny C., Bertsch D.L., Chiang J., et al., 1995, *ApJ* 440, 525
 Wagner S.J., Camenzind M., Dreissigacker O., et al., 1995, *A&A* 298, 688
 Waltman E.B., Fiedler R.L., Johnston K.J., et al., 1991, *ApJS* 77, 379
 Webb J.R., Smith A.G., Leacock R.J., et al., 1988, *AJ* 95, 374
 Wehrle A.E., Cohen M.H., Unwin S.C., et al., 1992, *ApJ* 391, 589
 Wehrle A.E., Unwin S.C., Zook A.C., 1994, In: Zensus J.A., Kellermann K.I. (eds.) *Compact Extragalactic Radio Sources*. Green Bank, WV: Natl. Radio Astron. Obs., p. 197
 Zensus J.A., 1997, *ARA&A* 35, 607